FERROELECTRICS

A stable rhombohedral phase in ferroelectric $Hf(Zr)_{1+x}O_2$ capacitor with ultralow coercive field

Yuan Wang[1,2]†, Lei Tao[3]†, Roger Guzman[3], Qing Luo[1,2]*, Wu Zhou[3], Yang Yang[1,2], Yingfen Wei[4], Yu Liu[1,2], Pengfei Jiang[1,2], Yuting Chen[1,2], Shuxian Lv[1,2], Yaxin Ding[1,2], Wei Wei[1,2], Tiancheng Gong[1,2], Yan Wang[1,2], Qi Liu[4], Shixuan Du[5,3,6]*, Ming Liu[1,2,4]*

Hafnium oxide–based ferroelectric materials are promising candidates for next-generation nanoscale devices because of their ability to integrate into silicon electronics. However, the intrinsic high coercive field of the fluorite-structure oxide ferroelectric devices leads to incompatible operating voltage and limited endurance performance. We discovered a complementary metal-oxide semiconductor (CMOS)–compatible rhombohedral ferroelectric $Hf(Zr)_{1+x}O_2$ material rich in hafnium-zirconium [Hf(Zr)]. X-ray diffraction combined with scanning transmission electron microscopy reveals that the excess Hf(Zr) atoms intercalate within the hollow sites. We found that the intercalated atoms expand the lattice and increase the in-plane and out-of-plane stresses, which stabilize both the rhombohedral phase (r-phase) and its ferroelectric properties. Our ferroelectric devices, which are based on the r-phase $Hf(Zr)_{1+x}O_2$, exhibit an ultralow coercive field (~0.65 megavolts per centimeter). Moreover, we achieved a high endurance of more than 10^{12} cycles at saturation polarization. This material discovery may help to realize low-cost and long-life memory chips.

The discovery of ferroelectricity in hafnium oxide (HfO_2) inspired a renewed interest in ferroelectric devices (*1*–*4*). Ferroelectric HfO_2 exhibits robust electric dipoles at nanometer thicknesses (*1*, *2*, *5*) and is compatible with modern complementary metal-oxide semiconductor (CMOS) technology (*6*, *7*). The compatibility with CMOS enables the realization of ultradense ferroelectric random-access memory (FeRAM), which makes FeRAM a competitive candidate for next-generation nonvolatile memory devices (*4*–*6*, *8*–*11*). Yet, the high coercive field (E_c) of ferroelectric Hf$(Zr)O_2$ (HZO), leading to a high operating voltage, is a key issue that inhibits the application of HZO-based FeRAM at the state-of-the-art technology node (*12*). Moreover, the applied electric field for remnant polarization (P_r) switching is around 60 to 80% of the breakdown strength, suggesting an inherently small margin in securing the allowed number of field cycles before the breakdown (*13*). This problem is intrinsic to the fluorite-structure oxides, in which domain walls do not propagate efficiently and can move only by hopping over a large energy barrier (*1*).

To decrease the E_c of the orthorhombic ferroelectric Hf$(Zr)O_2$ (o-phase HZO), the energy barrier between the $+P_r$ and $-P_r$ states can be lowered by increasing the stability of the intermediate state [the tetragonal phase of Hf$(Zr)O_2$ (t-phase HZO)]. A stable intermediate t-phase HZO will reduce the stability of the polarized o-phase and will lead to a lower P_r and longer wake-up cycling (*14*–*16*). However, different work-function electrodes can make the antiferroelectric hysteresis loop shift in one direction, so that the t-phase switches between positive (or negative) and nonpolarized states. This method can reduce E_c by one-half and improve endurance to 10^{10} cycles. Yet, the P_r of single-sided polarization reversal in this t-phase antiferroelectric material is only one-half of the o-phase HZO ($2P_r$ ~ 16 μC/cm^2) (*17*–*19*). The polarization switching of the r-phase depends not only on crystal polarization but also on extrinsic factors such as defect migration (*2*), which is different from that of the o-phase. Because of the high formation energy, the stability of stoichiometric r-phase HZO is dependent on the stress imparted by the structure of the electrode, which is obtained only through

[1]State Key Lab of Fabrication Technologies for Integrated Circuits, Institute of Microelectronics, Chinese Academy of Sciences, Beijing, China. [2]Key Laboratory of Microelectronics Devices and Integrated Technology, Institute of Microelectronics, Chinese Academy of Sciences, Beijing, China. [3]School of Physical Sciences, University of Chinese Academy of Sciences, Beijing, China. [4]Frontier Institute of Chip and System, Fudan University, Shanghai, China. [5]Institute of Physics, Chinese Academy of Sciences, Beijing, China. [6]Songshan Lake Materials Laboratory, Dongguan, China.
***Corresponding author. Email: luoqing@ime.ac.cn (Q.L.); sxdu@iphy.ac.cn (S.D.); liuming@ime.ac.cn (M.L.)**
†These authors contributed equally to this work.

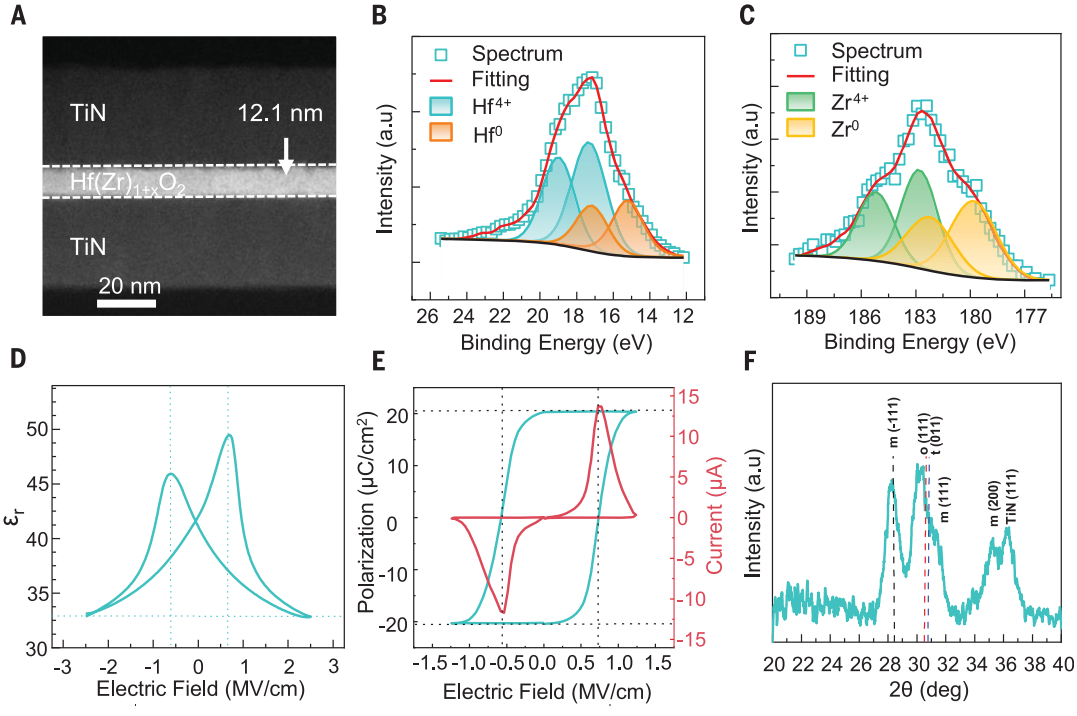

Fig. 1. Planar metal-ferroelectric-metal (MFM) capacitors and structural characterization of $Hf(Zr)_{1+x}O_2$ films. (**A**) Cross-sectional STEM-HAADF image of the TiN/Hf$(Zr)_{1+x}O_2$/TiN structure with a thickness of 12.1 nm. Scale bar, 20 nm. (**B**) The XPS spectrum of Hf 4f in Hf$(Zr)_{1+x}O_2$ film. (**C**) The XPS spectrum of Zr 3d in Hf$(Zr)_{1+x}O_2$ film. (**D**) Small signal CV hysteresis at 10 kHz (50-mV level) of 12-nm Hf$(Zr)_{1+x}O_2$ capacitors. (**E**) PUND measurements of Hf$(Zr)_{1+x}O_2$ capacitors under an electric field of frequency of 1 kHz. The red curve is the *I*-*E* curve after extracting the non-ferroelectric switching response; the blue curve is the integrated signal giving rise to the corresponding *P*-*E* hysteresis loop. (**F**) GIXRD spectra of TiN/Hf$(Zr)_{1+x}O_2$/TiN stack capacitors.

epitaxial growth (*4*). Therefore, a CMOS-compatible and stable HZO-based material in r-phase can not only fundamentally solve the dilemma of hafnia-based ferroelectric optimization but can also retain the advantages of HZO material.

We report a ferroelectric r-phase in a $Hf(Zr)_{1+x}O_2$ material and demonstrate a highly CMOS-compatible way for experimentally constructing the r-phase in HfO_2 materials by increasing the atomic ratio of Hf to O. We used x-ray diffraction (XRD) and scanning transmission electron microscopy (STEM) experiments to confirm the existence of the r-phase. Using a high-angle annular dark-field (HAADF) image of the $Hf(Zr)_{1+x}O_2$ film, we show the intercalation of excess Hf(Zr) atoms, confirming the Hf(Zr)-excess structure. Our density functional theory (DFT) calculations reveal that the formation energy of the r-phase is lower than those of the o-phase and monoclinic phase (m-phase) in Hf(Zr)-rich $Hf(Zr)O_2$ films when the ratio of Hf(Zr) to O is larger than 1.079:2, which is more conducive to the formation of the r-phase. We also conducted device experiments, which reveal a high P_r value of 22 μC/cm^2, a small saturation-polarization electric field (E_s) [1.25 megavolts (MV)/cm], an ultralow E_c (~0.65 MV/cm), and a high breakdown electric field (E_{BD}) (4.16 MV/cm). Moreover, we achieved a long device lifetime of more than 10^{12} cycles at saturation polarization.

Preparation and structural characterization of r-phase $Hf(Zr)_{1+x}O_2$

We fabricated and characterized metal-ferroelectric-metal (MFM) capacitors with $Hf(Zr)_{1+x}O_2$ films (thickness of 12 nm) to confirm their ferroelectricity. Ferroelectric $Hf(Zr)_{1+x}O_2$ layers can be simply obtained by using magnetron sputtering from Hf and ZrO_2 targets. We introduced a reactive oxygen source during sputtering (fig. S1). We show a cross-sectional STEM-HAADF image with the stacking of TiN/$Hf(Zr)_{1+x}O_2$/TiN layers (Fig. 1A). Using energy-dispersive x-ray spectroscopy (EDS) maps (fig. S2), we confirmed that the TiN/$Hf(Zr)_{1+x}O_2$/TiN device has structurally and chemically sharp interfaces without obvious interdiffusion. Our x-ray photoelectron spectroscopy (XPS) analysis of $Hf(Zr)_{1+x}O_2$ films confirms that the Hf(Zr) content in the film is greater than that of standard stoichiometry. When the Hf source power was varied, the x in $Hf(Zr)_{1+x}O_2$ films increased from 0.129 to 0.273 (fig. S3A). The depth-profile analysis of $Hf(Zr)_{1+x}O_2$ films shows that the elemental proportion of Hf, Zr, and O in the thin layer does not change with the thickness (fig. S3, B to D). A careful fitting of the spectra (Fig. 1, B and C) reveals that the Hf^{4+} and Zr^{4+} components in the film coexist with metallic Hf^0 and Zr^0. We observed characteristic small signal capacitance–voltage (*C-V*) curves in MFM capacitors (Fig. 1D), which is common. The dielectric constant of the r-phase $Hf(Zr)_{1+x}O_2$ film that we fabricated (ε_r = 33.15) is ~16.5% greater than that of the ferroelectric o-phase HZO film (fig. S4). To elucidate the ferroelectric properties of TiN/$Hf(Zr)_{1+x}O_2$/TiN samples, we performed the measurements using the positive-up-negative-down (PUND) technique (fig. S5). We show a typical hysteresis polarization versus electric field (*P-E*) loop of the TiN/$Hf(Zr)_{1+x}O_2$/TiN device after 550°C of rapid thermal annealing (Fig. 1E), indicating an ultralow E_c of −0.58 MV/cm and +0.73 MV/cm. We achieved a large P_r value of 22 μC/cm^2 at a small driving electric field of 1.25 MV/cm. The ε_r and E_c showed characteristics different from those of o-phase ferroelectrics. As a result, we carried out grazing incidence x-ray diffraction (GIXRD) on the $Hf(Zr)_{1+x}O_2$ film (Fig. 1F), which indicated that the polycrystalline sample contains both m-phase and r-phase. Typically, the reflection peaks of o(111) and t(011) of HZO films appear around 30.5° and 30.8°, respectively (*4*, *20*). However, the 2θ value of this $Hf(Zr)_{1+x}O_2$ film is slightly lower at around 30.1°. To further confirm the lattice structure of the $Hf(Zr)_{1+x}O_2$ thin film, TEM analysis of this $Hf(Zr)_{1+x}O_2$ film was necessary.

We show a high-resolution HAADF-STEM image of the Hf(Zr)-rich $Hf(Zr)_{1+x}O_2$ film viewed along the [1-21] zone axis (unless specified, we use rhombohedral notations for crystallography indices hereafter) (Fig. 2A). A close-up image

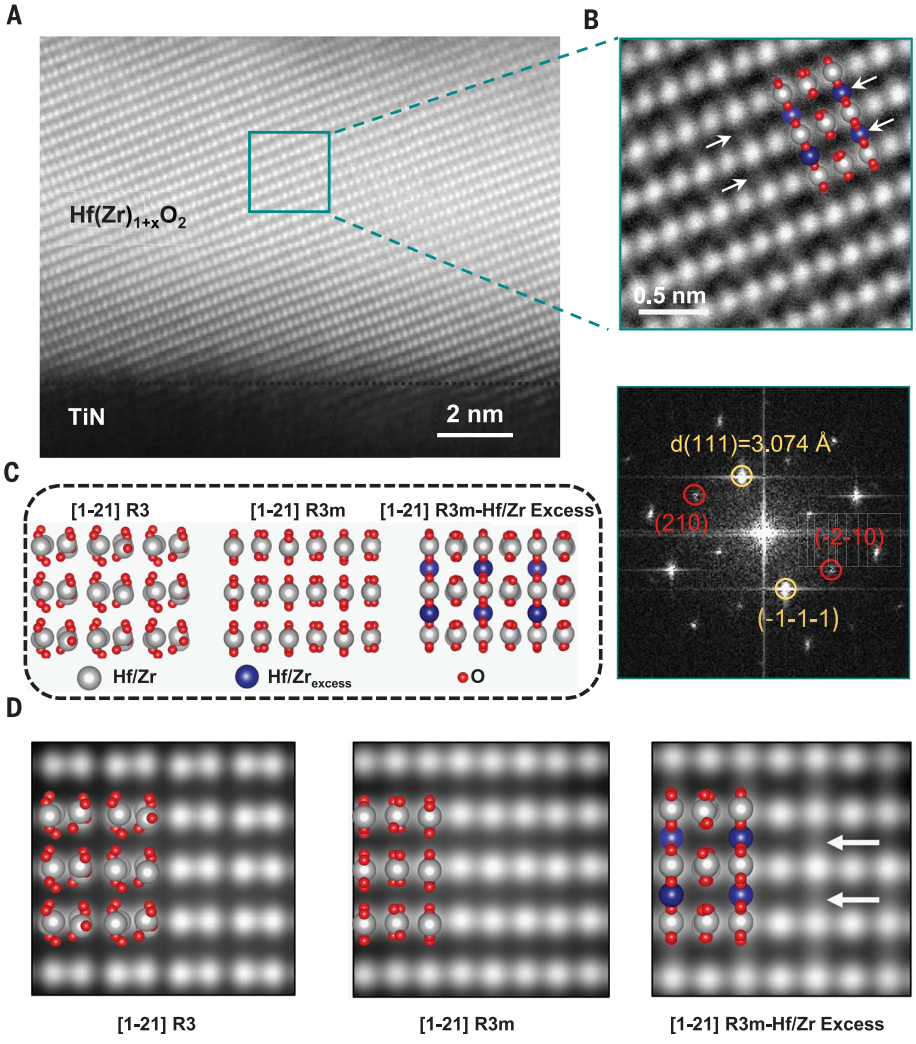

Fig. 2. Atomic-scale STEM analysis of the rhombohedral phase $Hf(Zr)_{1+x}O_2$. (**A**) Cross-sectional STEM-HAADF image of the $Hf(Zr)_{1+x}O_2$ structure along the [1-21] zone axis in rhombohedral notation. Scale bar, 2 nm. (**B**) (Top) Close-up image of the $Hf(Zr)_{1+x}O_2$ structure showing the intercalation of the excess Hf(Zr) atoms (highlighted by the white arrows). An atomic model is overlaid to guide the eyes. Scale bar, 0.5 nm. (Bottom) FFT of the close-up HAADF image. (**C**) Atomic models of HfO_2 with two kinds of rhombohedral structures and *R3m* structure with Hf excess ($Hf_{1+x}O_2$). (**D**) HAADF image simulations along the [1-21] zone axis for different structures. The extra contrasts arising from the excess Hf(Zr) atoms are highlighted by the white arrows.

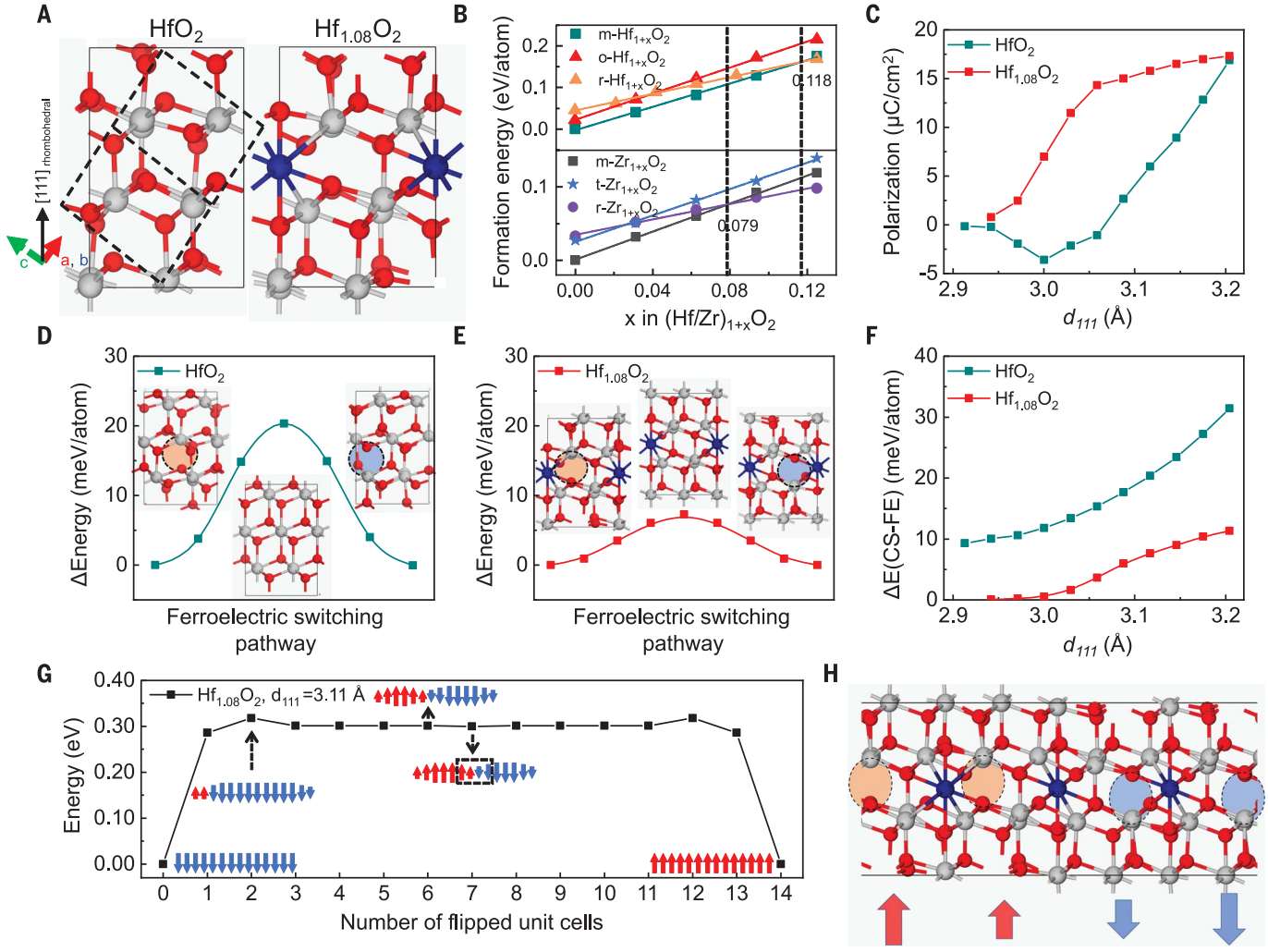

Fig. 3. Ferroelectric $Hf(Zr)_{1+x}O_2$ predicted by DFT calculations. (**A**) Atomic configurations of ferroelectric rhombohedral HfO_2 and $Hf_{1.08}O_2$. The extra Hf atom is marked in blue. The dashed line is the pristine rhombohedral lattice, and the solid lines are the hexagonal lattice. The [111] direction of the rhombohedral lattice is aligned with the *c* axis of the hexagonal lattice. (**B**) Formation energy of $Hf_{1+x}O_2$ in r-, o-, and m-phases as a function of *x* (upper) and $Zr_{1+x}O_2$ in r-, t-, and m-phases as a function of *x* (lower). The linear-fitted lines show the structural transition from orthorhombic $Hf_{1+x}O_2$ (tetragonal $Zr_{1+x}O_2$) to rhombohedral $Hf_{1+x}O_2$ ($Zr_{1+x}O_2$) is at 0.039 (0.025), and the transition from monoclinic to rhombohedral $Hf_{1+x}O_2$ ($Zr_{1+x}O_2$) is at 0.118 (0.079), indicating that the m-r phase transition for the binary $Hf(Zr)_{1+x}O_2$ occurs when the value of *x* is larger than 0.079. (**C**) Polarization of r-phase HfO_2 and $Hf_{1+x}O_2$ as a function of d_{111}. (**D** and **E**) Energy landscape showing the ferroelectric switching process of HfO_2 and $Hf_{1.08}O_2$ with d_{111} of 3.11 Å, respectively. (**F**) Energy differences (ΔE) between centrosymmetric (CS) r-phase $Hf_{1+x}O_2$ and ferroelectric (FE) r-phase $Hf_{1+x}O_2$ as a function of d_{111}. These energy differences represent the estimated ferroelectric barriers. (**G**) Energy landscape across the ferroelectric switching pathway in the 14-unit-cell-wide r-phase $Hf_{1.08}O_2$ with d_{111} of 3.11 Å as a function of the flipped unit cell. (**H**) Configuration of domain wall separating the 180° polar domains according to the black rectangle in (G).

(Fig. 2B) shows the intercalation of excess Hf(Zr) atoms into the structure, forming an ordered array within the hollow sites, which is in agreement with our Hf-excess model (Fig. 2C). Along this crystal projection, the occupation in the excess Hf(Zr) columns is about 1/6, thus the Z-contrast of the excess Hf(Zr) sites is weaker than that of the regular Hf(Zr) columns. Corresponding fast Fourier transform (FFT) in the lower panel of Fig. 2B perfectly matches with the simulated electron diffraction patterns of Hf-excess *R3m*[1-21] phase (fig. S6B). The d_{111} spacing that we directly measured from FFT is 3.074 Å. Then we compared the experimental FFT with those of the other structures in fig. S6C. The o-phase could be excluded, which is characterized by the extinction of (210) diffraction spots marked by the dashed red circles in the simulated electron diffraction pattern. To further confirm the Hf-excess structure, we performed HAADF image simulation of the *R3* phase, the *R3m* phase without excess Hf, and the *R3m* phase with Hf excess (Fig. 2D). The *R3* phase shows an obvious lattice modulation forming Hf-Hf dumbbells, which we did not observe in the other two structures, nor in our experiments. The image simulation of *R3m* structure with Hf excess is in agreement with the experimental observations. Figure S7 shows the intensity-line profile comparison between the experimental and the simulated structures, illustrating the contrast modulation within the hollow sites, which confirms the ordering of the Hf(Zr) excess atoms.

DFT calculations

The ferroelectric property of $Hf(Zr)O_2$ is believed to originate from the spontaneous centrosymmetry-breaking of the r-phase $Hf(Zr)O_2$, induced by the displacement of Hf(Zr) and corresponding O (fig. S8), and is closely related to the applied strain in the [111] direction. However, the formation energy of the r-phase $Hf(Zr)O_2$ is much higher than those of other phases. By using DFT calculations, we calculated the formation

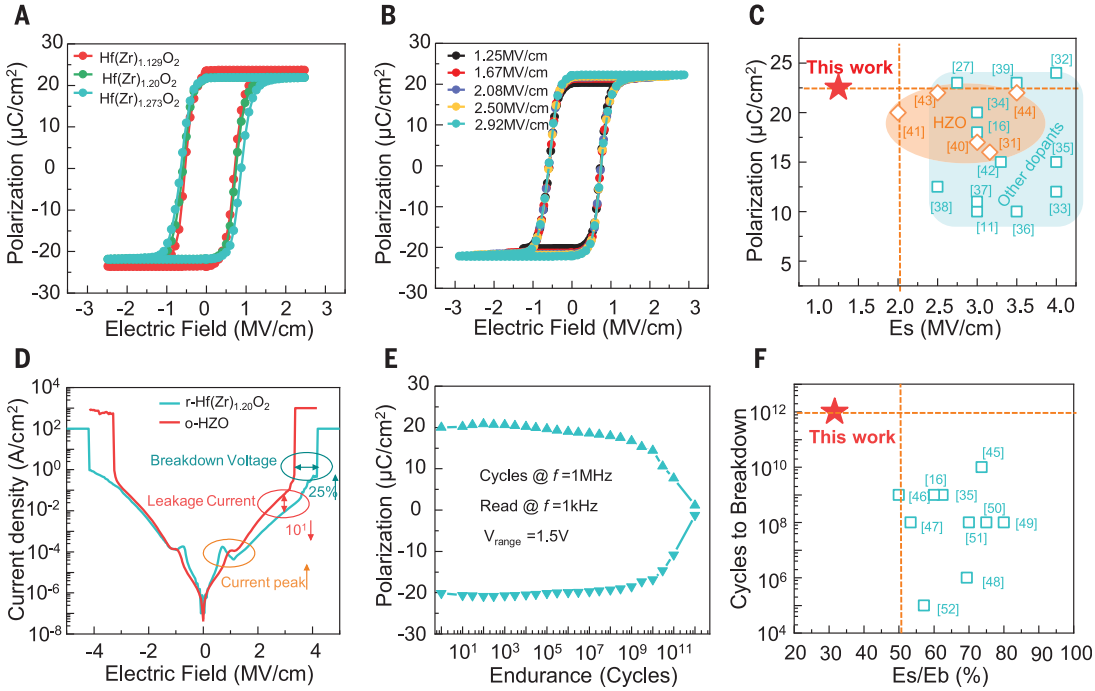

Fig. 4. Ferroelectric properties of r-phase $Hf(Zr)_{1+x}O_2$ films. (**A**) PUND measurements of r-phase $Hf(Zr)_{1+x}O_2$ capacitors prepared with different Hf powers under an electric field of frequency 1 kHz. (**B**) *P-E* curves of the r-phase ferroelectric $Hf(Zr)_{1.20}O_2$ capacitor at different electric fields. (**C**) Benchmarking of $Hf(Zr)_{1+x}O_2$ film reported in this work against some reported HfO_2-based ferroelectric films (*11*, *16*, *27*, *31*–*44*) with regard to E_s. (**D**) *I-E* characteristics of o-phase $Hf_{0.5}Zr_{0.5}O_2$ (HZO) ferroelectric thin films and r-phase $Hf(Zr)_{1+x}O_2$ ferroelectric thin films. (**E**) Endurance properties of the r-phase ferroelectric $Hf(Zr)_{1+x}O_2$ capacitor. (**F**) Benchmarking of HZO film reported in this work against some reported HfO_2-based ferroelectric films (*16*, *35*, *45*–*52*) with regard to endurance. Eb, breakdown electric field.

energies of the Hf-rich $Hf_{1+x}O_2$ in r-, o-, and m-phases, and Zr-rich $Zr_{1+x}O_2$ in r-, t-, and m-phases with increasing Hf(Zr) ratio (Fig. 3B). Using HfO_2/ZrO_2 instead of binary HZO to do the calculations is a common strategy, which has been widely used to estimate the formation energies in two extreme cases (*4*, *21*–*23*). We show the resulting atomic structure of stoichiometric r-phase HfO_2 (Fig. 3A, left) and $Hf_{1.08}O_2$ (Fig. 3A, right) with an extra Hf atom (blue balls) at the hollow site bonding to the neighboring oxygen atoms in a hexagonal supercell marked by solid lines. The r-phase becomes more stable than o-phase $Hf_{1+x}O_2$ when x is >0.039, whereas in $Zr_{1+x}O_2$, the value of x for r-t phase transition is 0.025 (Fig. 3B). When x is >0.079 for $Zr_{1+x}O_2$ and >0.118 for $Hf_{1+x}O_2$, the r-phase $Hf_{1+x}O_2/Zr_{1+x}O_2$ has the lowest formation energies, which are even lower than the ground state usually reported for the nonferroelectric m-phase, resulting in a ground-state ferroelectric $Hf_{1+x}O_2/Zr_{1+x}O_2$. Therefore, for binary HZO, the phase transition from m-phase to r-phase of $Hf(Zr)_{1+x}O_2$ should occur when the value of x is >0.079. We further verified the structural stability of $Hf_{1.08}O_2$ by calculating the phonon dispersion (fig. S9A). Although the excess Hf atoms will introduce extra strain in the lattice, the structure can be stabilized by forming a new phase with ordering Hf(Zr) excess atoms. Therefore, we used $Hf_{1.08}O_2$ in the simulation that follows. In addition, the formation energies of Hf interstitial with oxygen vacancy and antisite defect (fig. S10) indicate that the presence of Hf or Zr interstitials is unlikely to cause additional defects, such as oxygen vacancies. As x increases to 0.125, the r-phase $Hf_{1.125}O_2$ remains well ordered at room temperature (fig. S9B), indicating the robustness of ferroelectricity in r-phase $Hf_{1+x}O_2$. By contrast, the structure of o-phase $Hf_{1+x}O_2$ has almost lost its ferroelectricity owing to the random movement of the oxygen atoms (fig. S11) when x is 0.125.

The ferroelectric polarization in r-phase HfO_2 is believed to be induced by the lattice expansion in the [111] direction (*4*). The stoichiometric r-phase HfO_2 has a very small negative polarization if d_{111} is <3.06 Å (Fig. 3C). If d_{111} is >3.06 Å, the value of polarization of HfO_2 becomes positive and keeps increasing. After the intercalation of excess Hf atoms, the value of d_{111} becomes 2.94 Å for $Hf_{1.08}O_2$, which is 1% greater than that of stoichiometric r-phase HfO_2 (d_{111} = 2.91 Å). Therefore, the lattice expansion in the [111] direction of the r-phase $Hf(Zr)_{1+x}O_2$ not only comes from the electrode but also from the intercalation of excess Hf(Zr) atoms. Similarly to the stoichiometric r-phase HfO_2, the polarization of $Hf_{1.08}O_2$ depends on the value of d_{111}, in which the polarization increases to 15 μC/cm² with a d_{111} of 3.1 Å. The existence of Zr can stabilize r-phase $Hf(Zr)_{1+x}O_2$ (*24*) without changing ferroelectric properties substantially (figs. S12 and S13).

Our STEM experiment reveals that the ratio between the in-plane (−101) and out-of-plane (111) lattice parameters is ~1.14 when the $Hf(Zr)_{1+x}O_2$ sample is viewed along the [1-21] zone axis (figs. S6 and S15). This value is close to that of a structure with a d_{111} of 3.11 Å (ratio ~1.124) according to DFT calculations (fig. S14), which corresponds to a strain of ~7%. We show the ferroelectric switching pathway of 7%-strain $Hf_{1.08}O_2$, which has a switching barrier of only 7.6 meV per atom (Fig. 3, D and E). Comparing that with stoichiometric HfO_2, which has a barrier of 20 meV per atom, we find that the electric field for ferroelectric switching is much smaller in r-phase $Hf_{1.08}O_2$ than that in stoichiometric r-phase HfO_2. Although the switching barriers of both HfO_2 and $Hf_{1.08}O_2$ increase with d_{111} (Fig. 3F), the switching barrier of r-phase $Hf_{1.08}O_2$ is consistently much lower than that of r-phase HfO_2 at different d_{111}.

Unlike the ferroelectric HfO_2 in o-phase with localized dipoles, the ferroelectric $Hf_{1+x}O_2$ with spread dipoles has quite broad domain walls, which contribute to a low E_c. We show the energy landscape across the ferroelectric switching pathway in the 14-unit-cell-wide $Hf_{1.08}O_2$ with a d_{111} of 3.11 Å as a function of the flipped unit cell (Fig. 3G). The energy increases to 0.33 eV when two-unit-cell $Hf_{1.08}O_2$ is flipped and decreases to 0.29 eV after flipping four-unit-cell $Hf_{1.08}O_2$. The energy variation with more flipping unit cells indicates that the width of the domain wall in the r-phase $Hf_{1.08}O_2$ is at least 1.2 nm (two-unit cell of $Hf_{1.08}O_2$) and that the required energy for creating a 180° domain wall in the $Hf_{1.08}O_2$ is about 0.22 eV/nm². Figure 3H shows the domain-wall structure separating the 180° polar domains according to Fig. 3G, in which the polarization is suppressed substantially. These domain walls with spread dipoles in the r-phase $Hf_{1.08}O_2$ result in a relatively small ferroelectric switching barrier. We show the ferroelectric switching barriers in the broad domain wall (fig. S16) according to Fig. 3,

G and H. The barrier for flipping all the dipoles in each unit cell independently is 0.28 eV per unit cell including 37 atoms (7.6 meV per atom in Fig. 3E), whereas it is only 0.12 eV per unit cell in the domain wall (fig. S16B). Although this energy barrier is much smaller than that of the oxygen vacancies' migration (*25*), oxygen-vacancy migration is still possible during long-term electric field operation.

Electrical characterization of rhombohedral $Hf(Zr)_{1+x}O_2$

The process window is a key parameter of semiconductor technology (*26*, *27*). The larger the parameter is, the more conducive to the control of product yield (*26*). The r-phase $Hf(Zr)_{1+x}O_2$ ferroelectric thin films with the experimentally measured value of x >0.129 have good stability. For r-phase $Hf(Zr)_{1+x}O_2$ ferroelectric thin films prepared with different Hf power (Fig. 4A), although the x in $Hf(Zr)_{1+x}O_2$ films varied from 0.129 to 0.273 (fig. S3A), there was almost no change in the P_r value and E_c, with only 2.37 $\mu C/cm^2$ and 0.17 MV/cm variations of $2P_r$ and $2E_c$, respectively (fig. S17A). We measured the *P-E* curves of the r-phase ferroelectric $Hf(Zr)_{1.2}O_2$ capacitor at different electric fields (Fig. 4B). The $\Delta 2P_r$ and $\Delta 2E_c$ are only 3.2 $\mu C/cm^2$ and 0.01 MV/cm, respectively (fig. S17B). This indicates that the E_s of the r-phase ferroelectric $Hf(Zr)_{1+x}O_2$ capacitor is only 1.25 MV/cm, and thus we can achieve a large P_r value of 22 $\mu C/cm^2$. We measured the current versus electric field (*I-E*) curves of the r-phase ferroelectric $Hf(Zr)_{1+x}O_2$ capacitor with different Hf(Zr) compositions and different electric fields (fig. S17, C and D). Figure 4C summarizes the P_r and E_s of ferroelectric HfO_2–based films from the literature. The r-phase ferroelectric $Hf(Zr)_{1+x}O_2$ capacitor shows the minimum E_s. We also measured the *P-E* curves of r-phase $Hf(Zr)_{1.20}O_2$ films with different thicknesses (fig. S18). We only found a slight change in P_r value and E_c between 8.8- and 12.1-nm $Hf(Zr)_{1.20}O_2$ films. The P_r value of the 6.4-nm film decreases to 14 $\mu C/cm^2$, and its E_c (0.9 MV/cm) is slightly larger than those of other thicker films, indicating that the coercive field increases with decreasing film thickness (*28*). Moreover, we obtained more than 10 years of data retention at 85°C (fig. S19). The device-to-device variation of r-phase $Hf(Zr)_{1+x}O_2$–based ferroelectric capacitors has been studied by using the statistical distribution of *P-E* curves (fig. S20A). The distribution of $2P_r$ and $2E_c$ remains in a narrow range (fig. S20B), indicating small device-to-device variation. We show reproducibility data for r-phase $Hf(Zr)_{1.20}O_2$ ferroelectric capacitors in four manufacturing batches (fig. S21). Considering manufacturing process errors, we believe that the slight differences in P_r values and E_c between $Hf(Zr)_{1.20}O_2$ ferroelectric capacitors from different manufacturing batches are acceptable.

The limited number of field cycles of the o-phase ferroelectric HfO_2–based devices is a natural consequence of such films' high E_c relative to their breakdown field strength (*13*). Although reducing the operating electric field can prolong the device lifetime, incomplete polarization occurs, resulting in the reduction of the P_r value. This phenomenon is called the "P_r-endurance dilemma" (*13*). Therefore, the key to solve this problem is to reduce the E_c and E_s of HfO_2-based ferroelectric films. Compared with o-phase ferroelectric HfO_2–based films, r-phase ferroelectric $Hf(Zr)_{1+x}O_2$–based films have a smaller E_c and E_s as a result of their lower kinetic-energy barrier between the two spontaneous polarization states. The ferroelectric capacitors achieve saturation polarization at an ultralow electric field (1.25 MV/cm) because of their smaller coercive field, E_c. Another important factor affecting the reliability of ferroelectric HfO_2–based films is leakage current and E_{BD}. We plot the *I-E* curves of o-phase HZO ferroelectric and r-phase $Hf(Zr)_{1+x}O_2$ ferroelectric devices (Fig. 4D). The peak highlighted with an orange ellipse in the dc current voltage (*I-V*) curve shows a negative differential resistance–type behavior, suggesting that this peak is a result of a combination of polarization switching and ion-migration phenomena (*2*, *29*). Compared with the o-phase ferroelectric HfO_2 cell, the leakage current of the r-phase $Hf(Zr)_{1+x}O_2$ device is reduced by an order of magnitude at 3 V dc voltage, and its E_{BD} is increased by 25%. Moreover, the E_s/E_{BD} is about 30%, which is only one-half that of the o-phase HfO_2–based ferroelectric device. Therefore, an r-phase $Hf(Zr)_{1+x}O_2$ ferroelectric cell can obtain 10^{12} field cycles at 1.25 MV/cm (Fig. 4E). We also obtained the endurance performances at different electric fields (fig. S22). These plots indicate great optimization potential for the endurance of these devices (*30*). When compared with the cycles to breakdown at saturation reported in the literature (Fig. 4F), the cycles of our r-phase ferroelectric $Hf(Zr)_{1+x}O_2$–based films have been improved by about two orders of magnitude.

Conclusions

We reported a r-phase ferroelectric $Hf(Zr)_{1+x}O_2$ thin film. The proposed ground-state r-phase ferroelectric $Hf(Zr)_{1+x}O_2$ film solves the problem of high E_c inherent in o-phase ferroelectric HfO_2. Furthermore, these r-phase $Hf(Zr)_{1+x}O_2$ ferroelectric thin films are CMOS-compatible. HAADF-STEM imaging of the $Hf(Zr)_{1+x}O_2$ film shows the intercalation of excess Hf(Zr) atoms, confirming the Hf(Zr)-excess structure. The excess Hf(Zr) atoms expand the lattice of $Hf(Zr)_{1+x}O_2$ and produce greater in-plane and out-of-plane stress, which is more conducive to stabilizing ferroelectric properties. An ultralow coercive field is obtained owing to Hf embedding in HfO_2, which decreases the r-phase switching barrier and the spread of dipole-induced broad domain walls. High E_{BD}, large P_r, and good endurance are achieved in the proposed ferroelectric $Hf(Zr)_{1+x}O_2$ capacitor simultaneously. Consequently, the discovery of the r-phase $Hf(Zr)_{1+x}O_2$ ferroelectric films may contribute to realizing low-cost and long-life memory chips.

REFERENCES AND NOTES

1. H. J. Lee *et al.*, *Science* **369**, 1343–1347 (2020).
2. P. Nukala *et al.*, *Science* **372**, 630–635 (2021).
3. H. Mulaosmanovic, E. T. Breyer, T. Mikolajick, S. Slesazeck, *Nat. Electron.* **3**, 391–397 (2020).
4. Y. Wei *et al.*, *Nat. Mater.* **17**, 1095–1100 (2018).
5. S. S. Cheema *et al.*, *Science* **376**, 648–652 (2022).
6. X. Xu *et al.*, *Nat. Mater.* **20**, 826–832 (2021).
7. A. I. Khan, A. Keshavarzi, S. Datta, *Nat. Electron.* **3**, 588–597 (2020).
8. T. Mikolajick, S. Slesazeck, M. H. Park, U. Schroeder, *MRS Bull.* **43**, 340–346 (2018).
9. Y. Yun *et al.*, *Nat. Mater.* **21**, 903–909 (2022).
10. U. Schroeder, M. H. Park, T. Mikolajick, C. S. Hwang, *Nat. Rev. Mater.* **7**, 653–669 (2022).
11. T. S. Böscke, J. Müller, D. Bräuhaus, U. Schröder, U. Böttger, *Appl. Phys. Lett.* **99**, 102903 (2011).
12. T. D. Hadnagy, *Integr. Ferroelectr.* **18**, 1–17 (2006).
13. M. H. Park, Y. H. Lee, T. Mikolajick, U. Schroeder, C. S. Hwang, *MRS Commun.* **8**, 795–808 (2018).
14. A. G. Chernikova *et al.*, *ACS Appl. Mater. Interfaces* **10**, 2701–2708 (2018).
15. M. G. Kozodaev *et al.*, *Appl. Phys. Lett.* **111**, 132903 (2017).
16. M. G. Kozodaev *et al.*, *J. Appl. Phys.* **125**, 034101 (2019).
17. M. Pesic, in *2016 IEEE International Electron Devices Meeting (IEDM)*, San Francisco, CA, 3 to 7 December 2016 (IEEE, 2016), pp. 11.16.1–11.16.4.
18. M. Pesic *et al.*, *IEEE J. Electron Devices Soc.* **6**, 1019–1025 (2018).
19. M. Pesic, U. Schroeder, S. Slesazeck, T. Mikolajick, *IEEE Trans. Device Mater. Reliab.* **18**, 154–162 (2018).
20. B. Prasad *et al.*, *Adv. Electron. Mater.* **7**, 2001074 (2021).
21. R. Materlik, C. Künneth, A. Kersch, *J. Appl. Phys.* **117**, 134109 (2015).
22. S. E. Reyes-Lillo, K. F. Garrity, K. M. Rabe, *Phys. Rev. B Condens. Matter Mater. Phys.* **90**, 140103 (2014).
23. T. D. Huan, V. Sharma, G. A. Rossetti, R. Ramprasad, *Phys. Rev. B Condens. Matter Mater. Phys.* **90**, 064111 (2014).
24. A. El Boutaybi, T. Maroutian, L. Largeau, S. Matzen, P. Lecoeur, *Phys. Rev. Mater.* **6**, 074406 (2022).
25. N. Capron, P. Broqvist, A. Pasquarello, *Appl. Phys. Lett.* **91**, 192905 (2007).
26. X. Zhang, H. Chen, Y. Long, K. Wang, in *2020 31st Annual SEMI Advanced Semiconductor Manufacturing Conference (ASMC)*, Saratoga Springs, NY, 24 to 26 August 2020 (IEEE, 2020), pp. 1–8.
27. T. Schenk *et al.*, in *2013 Proceedings of the European Solid-State Device Research Conference (ESSDERC)*, Bucharest, Romania, 16 to 20 September 2013 (IEEE, 2013), pp. 260–263.
28. M. Materano *et al.*, *Appl. Phys. Lett.* **117**, 262904 (2020).
29. J. Scott *et al.*, *Integr. Ferroelectr.* **4**, 85–92 (1994).
30. T. Gong *et al.*, in *Symposium on VLSI Technology*, Kyoto, Japan, 13 to 19 June 2021 (IEEE, 2021), pp. 1–2.
31. J. Müller *et al.*, *Appl. Phys. Lett.* **99**, 112901 (2011).
32. J. Müller *et al.*, *J. Appl. Phys.* **110**, 114113 (2011).
33. S. Mueller *et al.*, *ECS J. Solid State Sci. Technol.* **1**, N123 (2012).
34. D. Martin *et al.*, *Adv. Mater.* **26**, 8198–8202 (2014).
35. P. Polakowski *et al.*, in *2014 IEEE 6th International Memory Workshop (IMW)*, Taipei, Taiwan, 18 to 21 May 2014 (IEEE, 2014), pp. 1–4.
36. K. Florent *et al.*, *IEEE Trans. Electron Dev.* **64**, 4091–4098 (2017).
37. T. C. U. Tromm *et al.*, *Appl. Phys. Lett.* **111**, 142904 (2017).
38. Y. Wang *et al.*, *IEEE Electron Device Lett.* **39**, 823–826 (2018).
39. C. Mart, K. Kühnel, T. Kämpfe, S. Zybell, W. Weinreich, *Appl. Phys. Lett.* **114**, 102903 (2019).
40. S. Zarubin *et al.*, *Appl. Phys. Lett.* **109**, 192903 (2016).

41. S. Migita, . *ECS Trans.* **80**, 247–252 (2017).
42. A. Chouprik *et al*., *ACS Appl. Mater. Interfaces* **10**, 8818–8826 (2018).
43. S. J. Kim *et al*., *Appl. Phys. Lett.* **112**, 172902 (2018).
44. T. Kim, M. An, S. Jeon, *AIP Adv.* **10**, 015104 (2020).
45. V. Gaddam, D. Das, S. Jeon, *IEEE Trans. Electron Dev.* **67**, 745–750 (2020).
46. S. Kundu *et al*., *Sci. Rep.* **5**, 8494 (2015).
47. J. Müller *et al*., in *2013 IEEE International Electron Devices Meeting*, Washington, DC, 9 to 11 December 2013 (IEEE, 2013), pp. 10.8.1–10.8.4.
48. T. Onaya *et al*., *ECS Trans.* **98**, 63–70 (2020).
49. F. Mehmood *et al*., *Adv. Mater. Interfaces* **6**, 1901180 (2019).
50. Y. Cai *et al*., *Appl. Sci.* **11**, 4295 (2021).
51. H. Joh, T. Jung, S. Jeon, *IEEE Trans. Electron Dev.* **68**, 2538–2542 (2021).
52. K.-T. Chen *et al*., in *2019 Electron Devices Technology and Manufacturing Conference (EDTM)*, Singapore, 12 to 15 March 2019 (IEEE, 2019), pp. 62-64.

ACKNOWLEDGMENTS

We thank L. Li, X. Zheng, and H. Hu for their assistance in experimental appointments and literature search. **Funding:** This work is supported by the National Key R&D Program of China (2022YFB3608400, 2018YFA0305800), the Beijing Outstanding Young Scientist Program (BJJWZYJH01201914430039), the National Natural Science Foundation of China (61888102), and the Strategic Priority Research Program of the Chinese Academy of Sciences (XDB44000000). **Author contributions:** M.L., S.D., Q.Lu., Yu.W., and L.T. conceived the idea and the project plan. Yu.W. and Y.L. synthesized the films. R.G. and Y.Y. prepared samples for TEM and performed the experiments, and R.G. analyzed the data under the supervision of W.Z. Yu.W. and Y.Y. performed XRD and XPS and analyzed the data. Yu.W. fabricated devices and tested their ferroelectric properties, and L.T. performed the first-principles calculations under the guidance of S.D. and analyzed the data with help from S.D. and Q.Lu. M.L., S.D., and Q.Lu. extensively helped in understanding the structure and symmetry of the films. W.Z. and R.G. provided useful insights all through the project. Yu.W., L.T., Q.Lu., and S.D. co-wrote the manuscript with feedback from all of the authors. **Competing interests:** The authors have Chinese patents related to this work (CN202210189807.9, CN202210189814.9, CN202210192395.4, CN202210192427.0, CN202210192396.9, and 202310886393.X). **Data and materials availability:** The data that support the plots within this article and other findings of this study are available from the corresponding author upon reasonable request.

SUPPLEMENTARY MATERIALS

science.org/doi/10.1126/science.adf6137
Materials and Methods
Figs. S1 to S23
References (*53*–*61*)

Submitted 2 November 2022; accepted 22 June 2023
10.1126/science.adf6137

A stable rhombohedral phase in ferroelectric $Hf(Zr)_{1+x}O_2$ capacitor with ultralow coercive field

Yuan Wang, Lei Tao, Roger Guzman, Qing Luo, Wu Zhou, Yang Yang, Yingfen Wei, Yu Liu, Pengfei Jiang, Yuting Chen, Shuxian Lv, Yaxin Ding, Wei Wei, Tiancheng Gong, Yan Wang, Qi Liu, Shixuan Du, and Ming Liu

Science, **381** (6657), .
DOI: 10.1126/science.adf6137

Editor's summary
Hafnium oxides are attractive as materials for computer memories and other applications because their ferroelectric properties persist even for very thin layers. However, the relatively large risk of breakdown is one of the limiting factors in commercialization. Y. Wang *et al*. discovered that adding more hafnium and zirconium atoms helps to stabilize the ferroelectric properties. This allows for many more cycles before failure due to a decrease in the field required for polarization switching. —Brent Grocholski